

Effects of chlorine in ash on the corrosion performance of Ni-based alloys in simulated oxy-fuel environment

Zuotao Zeng^{†*}, Ken Natesan[†], Zhonghou Cai[‡] and David J Gosztola[§]

[†] Applied Materials Division, Argonne National Laboratory, Argonne, Illinois, 60439, USA

[‡] Advanced Photon Source, Argonne National Laboratory, Argonne, Illinois, 60439, USA

[§] Center for Nanoscale Materials, Argonne National Laboratory, Argonne, Illinois, 60439, USA

ABSTRACT

Alloy materials can be severely degrade by corrosive gases and coal ash in service of coal power plant at high temperature. To better understand alloy corrosion in coal power plant, it is necessary to study the effect of each constituent from coal combustion on alloy corrosion. Chlorine-containing compounds in coal are corrosion-accelerating agents. The concentration of chlorine increases a lot in gas environment of oxy-fuel combustion due to the absence of airborne nitrogen gas acting as a diluent. The role of chlorine in ash corrosion is investigated in simulated oxy-fuel environments. Long time tests over 3000 hours were performed on various alloys at 750 °C. The degradation depth, weight change, and microstructural characteristics of oxide scales on Ni-based alloys are reported after exposure at 750°C in oxy-fuel combustion environment for over 3000h. Synchrotron nanobeam X-ray analysis was performed to evaluate the phase and chemical composition of the oxide layers on the alloy surface. Nanobeam X-ray and SEM analyses indicate that chlorine can modify the diffusion mechanism near alloy surface, thereby, increase corrosion rate.

KEYWORDS Ash corrosion, Chlorine, Oxy-fuel, Long term test.

1. INTRODUCTION

Fossil fuel-fired power systems based on oxy-fuel combustion have attracted broad attention recently due to the potential for increased efficiency and the separation and capture of CO₂ and other pollutants. Oxy-fuel combustion uses an enriched (95% or greater) O₂ stream instead of air for the combustion process. The removal of nitrogen from the gas stream feeding the combustion process results in an overall 75% decrease in flue gas volume and greatly reduced NO_x formation. CO₂ and other pollutants are also easy to be separated for further sequestration. A near zero-emission coal power plant can be developed by using the oxy-fuel combustion method. However, the corrosion behavior of alloy materials in the presence flue gasses from oxy-fuel combustion may be different compared to normal air combustion due to the higher concentrations of CO₂, SO₂, HCl, and H₂O resulting from the absence of airborne N₂ acting as a diluent [1]. Breakaway oxidation and carburization of alloys can be observed when the content of steam and CO₂ increase in gas environment [2-4]. Sulfur can diffuse through oxide scales on alloys and increase their corrosion rates in coal plants [5, 6]. Alloys can be severely attacked by

coal ash at high temperature [7-16]. In our previous papers, we have reported the effect of SO₂ and CaO on coal ash corrosion [14-16]. In this paper, the effect of chlorine on alloy corrosion is investigated.

There is almost no chlorine in U.S. Western coal but it does have a high alkali (sodium and potassium) content [17]. On the other hand, the average chlorine content in U.S. Eastern coal ranges from 283 to 1262 ppm [17]. With the installation of flue gas desulfurization (FGD) systems at most larger U.S. coal-fired power plants, operators are increasingly using lower-cost Eastern coal. Chlorine was reported to be corrosive for coal power plant and biomass combustion system [17-31]. The chlorine content in biomass is generally much higher than that in coal. Ash compositions and flue gases after biomass combustion are also different from those of coal combustion. Therefore, the mechanisms of chlorine corrosion for biomass combustion could be different from those that observed in coal combustion.

We have reported in our earlier studies that there is an incubation period for ash corrosion [14-16]. The corrosion rate after incubation period increase dramatically and the rate law change from parabolic within incubation period to linear after incubation period. The incubation periods for several candidate lots of alloys are longer than 1000h at 740 °C [14]. Usually, reaction rates decrease with decreasing temperature therefore, it can be assumed that the incubation time would be longer at lower temperatures. Coal power plant components are designed for operation for over twenty years. To obtain reliable data for long term operation, corrosion test should be performed over 1000h. However, most recent reports on the effect of chlorine corrosion usually test only short-term (test time < 1000h) to evaluate alloy performance. Therefore, there are some conflicting results/interpretations of the effect of chlorine on alloy corrosion [17-31]. It is necessary to perform long term tests for understanding the effect of the chlorine on alloy corrosion, relevant to assessing the performance of in-plant components.

2. EXPERIMENTAL SECTION

2.1 Alloy Materials

To achieve high efficiency, alloy materials are required to possess adequate strength at temperatures above 700°C. High-Ni alloys (333, 617, 625, 230, 693, 740, and 718) are selected for test. Table 1 shows the compositions of the alloys selected for the study.

Table 1. Alloy nominal composition (in wt.%)

Alloy	Fe	Cr	Ni	Mn	Si	Mo	C	Other
333	18.0	25.0	45.0	-	1.0	3.0	0.05	Co 3.0, W 3.0
617	0.9	21.6	53.6	0.1	0.1	9.5	0.08	Co 12.5, Al 1.2, Ti 0.3
625	2.5	21.5	Bal	0.3	0.3	9.0	0.05	Nb 3.7, Al 0.2, Ti 0.2
230	1.2	21.7	60.4	0.5	0.4	1.4	0.11	W 14, Al 0.3, La 0.015
693	5.8	28.8	Bal	0.2	0.04	0.13	0.02	Al 3.3, Nb 0.67, Ti 0.4, Zr 0.03
740	1.0	25.0	Bal	0.3	0.5	0.5	0.07	Co 20.0, Ti 2.0, Al 0.8, Nb+Ta 2.0
718	19.0	19.0	52.0	-	-	3.0	-	Nb 5.0, Al 0.5, Ti 0.9, B 0.002
WASP	2.0	20	Bal	0.5	0.75	4.3	0.02	Co 12-15, Ti 2.6-3.25, Al 1.0-1.5, Zr 0.1

2.2 Gas Composition

An SO₂ concentration of 0.99% consistent with U.S. Eastern coal (may be blended) with intermediate sulfur content was used for this study since the SO₂ content in oxy-fuel combustion system is high [32, 33]. The variation of chlorine concentration in US coal is large. The average concentration of chlorine in US coal varies from 73ppm in PRB-powder River coal (US Western coal) to 1262ppm in Appalachian coal (US Eastern coal) [17].

Most chlorine leaves the boiler with the flue gas as HCl [34]. Two gas mixtures are used in this study to investigate the effect of chlorine on alloy corrosion. Their compositions are shown in Table 2. The concentrations of H₂O, CO₂, O₂, and SO₂ are the same in both gases. No HCl was added in Gas A. 200ppm HCl was used in Gas B to simulate the flue gas of the US Eastern coal in our experiment. Alloy performance in the gas environments A and B was compared to study the effect of HCl on alloy corrosion.

Table 2. Gas compositions for experiments

Gas #	H ₂ O (%)	CO ₂ (%)	O ₂ (%)	SO ₂ (%)	HCl (ppm)
A	26.9	68.14	3.97	0.99	0
B	26.9	68.14	3.97	0.99	200

2.3 Synthetic Ash Experiments

Ash compositions of U.S. Eastern coal and Western coal are different. The detail procedures to prepare the simulated ashes were reported in our previous paper [15]. The compositions of the two ashes are shown on Table 3.

Table 3. Ash compositions

Ash ID	Simulated condition	CaO (wt%)	SiO ₂ (wt%)	Fe ₂ O ₃ (wt%)	Al ₂ O ₃ (wt%)	Na ₂ SO ₄ (wt%)	K ₂ SO ₄ (wt%)
Ash E	U.S. Eastern coal	0	30	30	30	5	5
Ash W	U.S. Western coal	29	36	9	16	5	5

2.4 Corrosion Test

A tube furnace was used for corrosion tests. The reaction chamber was fabricated from a 5 cm ID alumina tube. Gas inlet/outlet fittings with specially designed flanges with O-ring seals were used at both end of the reaction chamber. A thermocouple was inserted to the zone with samples to monitor the specimen temperature from one end of the reaction chamber. The temperature of samples was controlled to within $\approx 3^\circ\text{C}$.

Figure 1 shows the experimental schematic to conduct steam and gas flows. High-purity CO₂, O₂, and SO₂ gases were piped into the reaction chamber through flowmeters to obtain the desired composition. Distilled water or HCl-water solution at the desired concentration was pumped into the tube furnace from a micro-metering water pump. The HCl-water solution was converted to steam and HCl gas in a preheater chamber. The coaxial-design mixing chamber enabled the steam and HCl to mix with the other gases.

Ash was contained in an alumina boat, and the alloy samples were buried in the ash. To obtain the data of weight change vs time, the corrosion tests were stopped every 300 h. The specimens were cleaned of the ash by brushing after cooling, and weighed. Corrosion tests were then continued with a fresh supply of the ash mixture.

2.5 Characterization of Samples

The thickness of each alloy specimen was measured before experiment. After corrosion test, the alloy specimens were cut to cross-section. A Hitachi S-4700-II scanning electron microscope (SEM) equipped with an energy dispersive X-ray analyzer was used to examine the samples. Thickness of scales and corrosion depth of the alloys were measured.

We carried out synchrotron X-ray fluorescence and diffraction measurement at the D end station of the sector 2 beamline in the Advanced Photon Source at Argonne National Laboratory. The X-ray beam of the size of 200nm in vertical and 300nm in horizontal was achieved by employing Fresnel zone plate focusing optics. Filtered with a silicon double crystal monochromator, the focused X-ray beam had a relative wavelength dispersion ($d\lambda/\lambda$) of better than 10^{-4} . Undulator X-ray source, combined with the high resolution monochromator and the advanced focusing lens, delivered 5×10^9 monochromatic photons per second into the focal spot. The X-ray beam was focused at the rotation center of the diffraction goniometer. As the sample is aligned into the sample rotation center, the minimum spot was intercepted with the surface of the specimen. We used 8.5 keV x-rays for the micro-XRD experiment. Iron-fluorescence signal was used to locate the oxide-metal interface as the sample was scanned across the beam.

Raman spectra and spectral area maps were recorded using an automated Raman microprobe (inVia, Renishaw, Inc.). Typical acquisition parameters were 514.5 nm excitation at 5 mW and 10 s signal integration/spectrum. A 50X, 0.75NA objective (Leica) was used in 180° back-scattering geometry for sample illumination/scattered light collection. For area maps, the sample was moved in 2 μm increments between spectral acquisitions.

3. RESULTS AND DISCUSSION

3.1. Alloy Weight Change and Incubation Period

Corrosion tests were conducted at 750°C in the presence of ash and oxy-fuel gases for a total exposure time over 3000 h. Tests for some alloys such as Alloy 693 were conducted up to 6300h. The weight loss data are shown in Figure 2 for all alloys after exposure to Ash E in Gas B at 750°C. Since different alloys contain varying constituent elements, the reaction between these alloy materials and ash can vary widely. Alloys generally lost weight after exposure to oxy-fuel

gas and ash at 750°C. The presence of chlorine in the gas feed increased weight loss rates of all Ni-based alloys tested. During the early period, the weight loss rates of several alloys are low (Figure 2). This period is referred as an incubation period. The corrosion rate accelerated upon exceeding the incubation period. Before incubation time, the corrosion rate law follows parabolic kinetics, but it changes to linear kinetics after incubation period.

The incubation time of alloys with high Cr content such as 693 are generally long (from 600h to 4200h). The incubation times for alloys with W, Mo and Nb are short (from 100h to 1000h). The effect of chlorine on the incubation time depended on the alloy composition, and the incubation time widely varied, based on the tests conducted in the environments with and without HCl (Figure 3). HCl addition reduced the incubation time for most Ni-based alloys.

The corrosion of some alloys was found to be localized in the ash environment. Figure 4 shows that localized attack on Alloys 740 and 693. Pits are observed on the surface of Alloy 740 after exposure to Gas B at 750 °C. However, the surface at some locations on Alloy 740 is still smooth after 2400h exposure. In evaluating alloy performance in an ash-containing environment of coal power plant, the depth of penetration rate is more important than the weight loss rate. It is necessary to develop the appropriate methodology for analyzing the ash corrosion data. In coal power plants, alloy components should be used for years. The corrosion rate after incubation time is a useful data to evaluate the alloy performance in ash corrosion environment. Therefore, we use the following equation to calculate the long-term corrosion rate:

$$r = \frac{d}{t - IT} \quad (1)$$

where r is the long-term corrosion rate (mm/year), d is the corrosion depth (mm), t is the total exposure time, and IT is the incubation time.

3.2. Effect of Gas and Alloy Composition on Ash Corrosion Rate

The initial thickness of the alloy plates was measured before corrosion tests. The corrosion rates of several alloys are low, and their original surfaces were still present in the localized ash corrosion. The original surface was used as the reference point for these samples. The corrosion rates are high for some samples, and their original surfaces were lost after heavy corrosion. In these cases, the thicknesses of the alloys at the location with the deepest corrosion depth were measured. Following equation is used to calculate the maximum corrosion depths.

$$d = (t_o - t_{rm})/2 \quad (2)$$

where d is the maximum corrosion depth, t_o is the original metal thickness measured before test, and t_{rm} is the minimum remaining metal thickness. After the maximum corrosion depth (d) and the incubation time (IT) were obtained, the long-term corrosion rate (r) can be calculated according to equation (1).

Figure 5 shows the corrosion rate of alloys in Gases A and B with the presence of Ash E at 750°C. The corrosion rates of most Ni-based alloys in HCl environment are much higher than those in

the gas environment without HCl. The corrosion rates for the alloys generally ranged between 1.9 and 9.1 mm/y after exposure to gas with HCl. The corrosion rate of Alloy 693 is the lowest (1.9 mm/y), and the rate of Alloy WASP is the highest. Among these alloys, the Cr content in Alloy 693 is the highest. Therefore, high Cr content is helpful to resist ash corrosion in the presence of chlorine. In the absence of HCl, Alloy 740 was the best to resist ash corrosion among the Ni-based alloys [14-15]. However, its corrosion rate increased significantly when the gas contained HCl.

Figure 6 shows that the grain boundaries of Alloy 740 were attacked after exposure to gas with HCl for 1200h at 750 °C. However, we did not observe a similar attack in the SEM image of Alloy 740 after exposure to gas without HCl. The penetration rate for Alloy 740 is ~ 3 times higher when it was exposed to gas with HCl than that without HCl. It seems that chlorine can increase grain boundary attack on alloys. EDX mapping analysis of Alloy 740 revealed that oxygen penetrates deeply into Alloy 740 along the grain boundary (Figure 7). However, the sensitivity of the EDX was not high enough to show the distribution of chlorine in the map since the concentration of chlorine in the gas feed was only 200ppm. Further study is needed to evaluate the role of chlorine in this process.

Alloys are usually protected by surface oxide scales that develop upon exposure to the gas environment. The oxide scale may consist of several layers. The phase composition of each layer cannot be determined by the conventional X-ray diffraction (XRD) since the beam size (>2mm) of conventional X-ray is too large. The synchrotron X-ray nano-beam can be focused to small size of 200-300nm. Therefore, we used the synchrotron X-ray nano-beam at the Argonne APS to scan across a cross-section of the alloy near its surface to analyze the phase composition of oxide scales on alloys.

The outer layer contained Ni, Fe, Co and Cr (Figure 8). Although the Fe and Ti contents in the bulk of Alloy 740 were very low, both elements were found to have diffused outwards and accumulate on the surface. Potassium content dropped rapidly with distance from the surface showing that the oxide scale successfully resisted inward diffusion of potassium. Figure 9 shows that the primary phase of the outer layer was $(\text{Ni, Cr, Co, Fe})_3\text{O}_4$ spinel from nano-beam X-ray diffraction analysis. The primary phase of the middle layer was Cr_2O_3 . The content of Cr increased dramatically in this layer (Figure 8). However, the spinel phase was also observed in this layer. The inner-most layer was the Cr depleted layer. Chromium diffused outward during oxidation, which led to lower Cr content in this layer.

Raman scattering was also used to study the phases in different layers of oxide scales. Raman spectra were obtained by focusing the laser beam on the different layers in oxide scale. Figure 10 shows 551 and 705 cm^{-1} bands emanating from the area without pits. The 551 cm^{-1} band is due to Cr_2O_3 [35,36] whereas the 705 cm^{-1} bands are due to the $(\text{Fe,Co,Cr})_3\text{O}_4$ spinel [37,38]. The outer layer consisted of almost pure spinel. However, the middle layer contained both Cr_2O_3 and spinel phases. These results are consistent with our nano-beam X-ray diffraction analysis.

Figure 11 shows the synchrotron nano-beam X-ray near edge absorption spectra near alloy surface. The chemical shifts of nickel in the outer and middle layers are close to NiO (Figure 11A). At the outer layer, the chemical shift of cobalt is higher than that of CoO (Figure 11B).

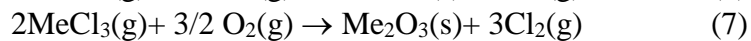
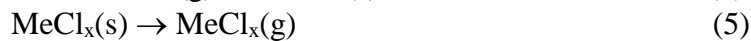
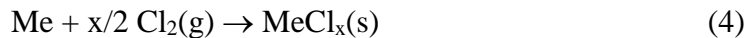
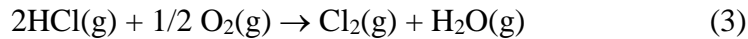
However, at inner layer, the chemical shifts of cobalt and nickel is close to cobalt and nickel metals respectively. Therefore we conclude that the oxidation state of nickel is +2 at the outer and middle layers, the oxidation state of cobalt is higher than +2, and Ni and Co are both metallic at the inner layers.

Sulfur can diffuse inward through oxide scales. X-ray fluorescence indicates that the sulfur contents at the outer and middle oxide layers are low. Its concentration increases in alloy near the boundary of oxide-metal. Sulfidation occur in alloy near the boundary of oxide-metal and consume metallic chromium. The SO₂ concentration in an oxy-fuel combustion system is much higher than in an air combustion environment [7]. It has been reported that high SO₂ content in oxy-fuel environment leads to high corrosion rate of alloys [14]. Therefore, sulfidation also plays an important role on the ash corrosion.

3.3. Chlorine-induced Corrosion Mechanism

Generally, there are two types of chlorine-induced corrosion mechanisms. One is related to a gas-solid reaction and the other is a liquid-solid reaction.

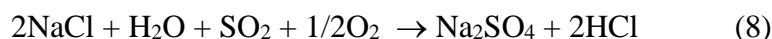
Grabke proposed an active oxidation mechanism for low alloy steel [39]. The mechanism involves the following gas-solid reactions:



Where *Me* is Fe, Cr, and Ni. HCl can be oxidized to Cl₂ according to Reaction (3). In the next step, chlorine gas penetrates the oxide scale through pores or cracks and reacts with alloy elements to form metal chlorides at the metal/scale boundary as shown in reaction (4) for CrCl₂(s). The boiling point of CrCl₂ is 1302 °C and has a high vapor pressure. The CrCl₂ vapor can diffuses through the cracks and pores of the oxide scale. According to reactions (6) and (7), CrCl₂ vapor can be oxidized and release chlorine. The cycle can be repeated to lead to active oxidation. The phases in the active oxidation are solid and gases. However, the difference between our experimental conditions and Grabke's experiment is that there is ash in our experiment. We have reported that K₃Al(SO₄)₃ is a stable melt in oxy-fuel environment at 750°C. The liquid phase in oxide scale can dramatically increase chlorine diffusion process.

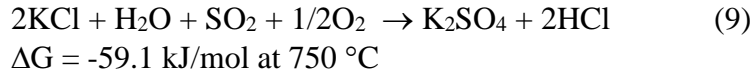
Frandsen et al proposed that KCl and NaCl can form a melt with K₂SO₄ and other salts [19,20] in biomass combustion environment. The low melting temperature eutectic can lead to hot corrosion. This model is identified as chloride-sulfate melt model. Oxide scale can dissolve into molten salt and increase the corrosion rate. However, our experimental conditions are different from the biomass combustion environment since US Eastern coal contains significant amount of sulfur. The following reactions are operative when there is significant sulfur in the gas environment.

For the reaction:



$$\Delta G = -64.58 \text{ kJ/mol at } 750 \text{ }^\circ\text{C}$$

The free energy of Reaction (8) is negative at 750 °C, the equilibrium constant for this reaction is $K = 1.98 \times 10^3$



For the reaction (9), the free energy is also negative at 750 °C. The equilibrium constant of this reaction:

$$K = 1.04 \times 10^3$$

The concentration of HCl is only 200 ppm in the gas feed in contrast, the concentration of H₂O, SO₂ and O₂ are 26.9%, 0.99%, and 3.97% respectively. The concentration of HCl on the right side of reaction (8) and (9) is much less than the concentration of H₂O, SO₂ and O₂, and the equilibrium constant of this reaction is large. Therefore, Na₂SO₄ and K₂SO₄ should be the primary alkali-containing components in the system and consequently, the concentration of NaCl and KCl should be very small at equilibrium. Since there is very little NaCl and KCl in the ash, the mechanism proposed by Frandsen *et al.* is not operative and cannot be effectively used to explain the results from our measurements [19,20].

Figure 12 shows that the difference between the models. For Grabke's active oxidation model, chlorine gas diffuses in and chloride gases diffuse out through the open pores in oxide scales. For the chloride-sulfate melt model, there is a liquid KCl-K₂SO₄ phase that is absorbed by capillary effect thus filling the open pores in the oxide scale. However, under our experimental conditions, the primary phase is K₃Al(SO₄)₃, instead of KCl-K₂SO₄. Furthermore, Cl₂ is a non-polar covalent molecule and generally, non-polar covalent gases are difficult to dissolve into ionic liquids. Experimental results have indicated that the diffusion rate of the polar covalent molecule: HCl is ten times higher than that of Cl₂ through molten salt [40,41]. If Cl₂ diffusion is blocked, the active oxidation mechanism does not work. Therefore, both the active oxidation mechanism and KCl-K₂SO₄ melt mechanism do not totally fit for our experimental conditions. However, our experimental results indicate that the corrosion rate increases in the presence of chlorine. It is necessary therefore to reevaluate the mechanism of chlorine-induced corrosion.

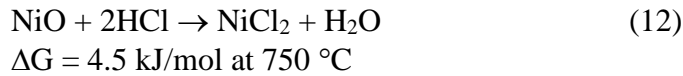
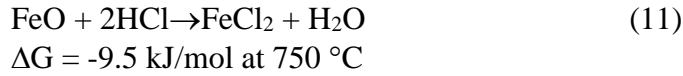
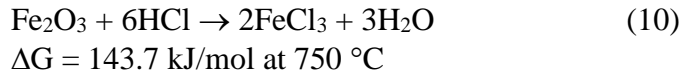
X-ray nano-beam analysis indicates that chlorine accumulates at the boundary of alloy and the oxide scale (Figure 8), which could cause the corrosion shown in Figures 6 and 7. Similar phenomenon was reported by other researchers. J. W. Rouse has done an Auger experiment on the oxidation of silicon assisted by HCl [42]. A thin layer of 10Å chlorine was observed at the boundary between oxide scale and silicon when the gas stream contained chlorine. In our measurements, it seems that chlorine can assist the transport of oxygen deep into the grain boundary. Aluminum oxide was observed at grain boundaries near the surface of Alloy 740 after exposure to ash and gas containing chlorine. The combination of X-ray nano-beam and SEM analyses indicates that the corrosion mechanism is related to chlorine-induced oxidation along grain boundaries of alloys with chromium outward diffusion being blocked after each grain is separated by oxides along grain boundaries.

The phase composition of the oxide scale formed in an ash environment containing chlorine is different from that in an ash environment without chlorine. Previously we reported the phase composition of the oxide scale of Alloy 740 formed in an ash environment without chlorine where one layer that consisted of almost pure Cr_2O_3 was observed underneath a spinel layer [14]. The Cr_2O_3 layer is much better than the spinel layer at resisting high temperature oxidation [4, 43]. However, we cannot find such a pure Cr_2O_3 layer in the oxide scale of Alloy 740 after exposure to the gas environment containing chlorine. The layer immediately above the alloy is a mixture of Cr_2O_3 and spinel (Figure 9 and Figure 10). Spinel is not as good as Cr_2O_3 at protecting the alloy from high temperature oxidation because the diffusion rate of oxygen through spinel is much faster than that through Cr_2O_3 [4, 43]. The presence of chlorine can therefore change the diffusion mechanism near the alloy surface, and thus increase the rate of corrosion. It is apparent that there is not sufficient chromium to form the Cr_2O_3 layer once the chromium outward diffusion path way is blocked by the formation of Al_2O_3 within the grain boundaries. The loss of a pure Cr_2O_3 layer decreases the incubation time of Alloy 740 and increases its corrosion rate. This mechanism is different from the active oxidation mechanism, which is related to a gas-solid reaction. Our proposed mechanism is also different from the chloride-sulfate melt mechanism, in which chlorides directly act as a component to form low melting temperature liquid phases and lead to hot corrosion. The chloride-sulfate melt mechanism is generally used to explain chlorine induced corrosion in biomass combustion, where the concentration of chlorides is very high. In our test environment, the concentration of chloride is not high enough to lead to the formation of a low melting point liquid phase. However, HCl can still diffuse through a salt melt and accumulate at the metal-oxide boundary. It seems that there is a cooperating mechanism between chlorine and oxygen diffusion because it is observed that oxygen deeply diffuses into alloys and accumulates at grain boundaries when chlorine is present at the boundary of the alloy and oxide. The accumulation of oxide at grain boundaries blocks the pathway for chromium outward diffusion preventing a pure Cr_2O_3 layer from forming at the metal-oxide interface, leading to rapid corrosion. Therefore, in our mechanism, chlorine does not act as a component for melt formation as in the chloride-sulfate melt mechanism, but rather it can affect the diffusion mechanism and change the phase composition of the oxide scale. Further study is needed to evaluate the role of chlorine in oxygen inward diffusion into grain boundaries of alloys.

3.4. Effect of CaO Addition on Ash Corrosion Rate

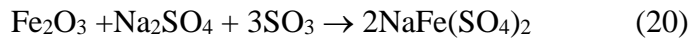
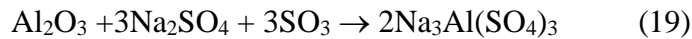
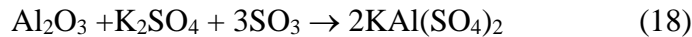
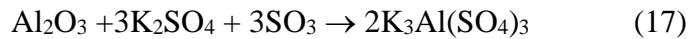
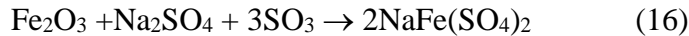
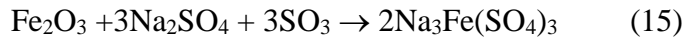
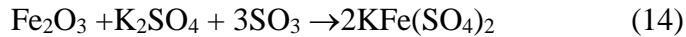
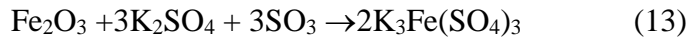
When Ash E (without CaO) was replaced by Ash W (with CaO), weight loss rates of alloys generally reduced after exposure to ash and Gas B (with HCl) at 750 °C (Figure 13). The weight loss rates for Alloys 333, 693, and 740 were lower than the other alloys. As noted in the previous section, when HCl was added to the gas environment and alloys were exposed to Ash E (without CaO), incubation times of alloys greatly decreased. However, incubation times for alloys exposed to Ash W (with CaO) and Gas B (with HCl) are generally longer than those exposed to Ash E (without CaO) and Gas B (with HCl) at 750 °C (Figure 14). Therefore, CaO addition increases the incubation time in the gas environment containing HCl. Figure 15 shows that the corrosion depths generally decrease after CaO addition into ash in the gas environment with HCl.

In these test series, the temperature and gas compositions are the same. Therefore, the addition of CaO to ash obviously reduces corrosion rate. Calcium compounds can react with other corrosion products and change the corrosion mechanism.



Reactions (10) and (12) are difficult since the free energy is positive and the concentration of HCl is low. However, in the micro-pore of oxide scale, selective absorption of HCl may lead to a higher concentration of HCl and may be high enough to form FeCl₂ through Reaction (11).

The multiple reactions between the ash and gas and alloy constituents lead that ash corrosion is much more complicated than that without ash. Various elements in these alloys can also participate reactions. For example, Alloys 625, 617, WASP, 718, and 333 contain Mo; Alloys 740, 617 and WASP contain Co; Alloy 230 and 333 contain W. Alloy 718 and 625 contain Nb; Alloy 693, 740, 617, WASP, 718 contain Al. Ash and gas can react with these elements in each alloy. Besides reacting with HCl, these oxides can also react with sulfur oxides to form low melting temperature compounds.

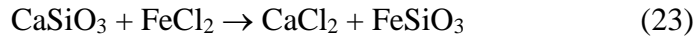


If compounds with low melting temperatures form, the alloy corrosion rate will increase. Table 4 shows some sulfates and chlorides with low melting temperature.

Table 4. Melting temperature of some chlorides and sulfates

Compounds	K ₂ SO ₄	Na ₂ SO ₄	CaCl ₂	FeCl ₂	Na ₃ Al(SO ₄) ₃	Na ₃ Fe(SO ₄) ₃	K ₃ Al(SO ₄) ₃	K ₃ Fe(SO ₄) ₃
Melting Temp (°C)	1069	884	772	677	646	624	654	618

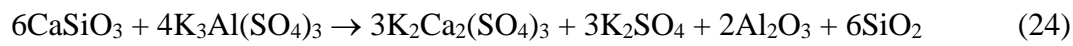
The melting temperature of FeCl₂ is lower than 750 °C so its presence could destroy oxide scales and lead to rapid corrosion [17, 39]. However, if there is CaO in the ash, it can react with HCl and scavenge the chloride as shown in reaction (23).



$$\Delta G = -14.9 \text{ kJ/mol at } 750 \text{ }^\circ\text{C}$$

Although the melting temperature of CaCl₂ is only 772°C, it can further react with Al₂O₃ and SiO₂ in ash to form Ca₁₂Al₁₄O₃₂Cl₂, Ca₂SiO₃Cl₂, Ca₃Al₂Si₂O₈Cl₄, and many other Ca-Al-Si-O-Cl compounds. Generally, the melting temperatures of chlorides are low compared to the melting temperatures of oxides because M-O⁻² bonds are typically much stronger than that M-Cl⁻¹ bonds. The melting temperatures of oxy-chlorides are also much higher than pure chlorides since the metal-oxide skeletons are strong even though a small amount of Cl⁻ is inserted into oxide lattice. These oxy-chloride compounds are solid phases below 1000 °C. Therefore, the formation of chloride phases with low melting temperature can be retarded by CaO addition. Additionally, the ionic conductivity of Ca₁₂Al₁₄O₃₂Cl₂ was found to be very low [44] thus the mobility of chlorine is limited by adding CaO into ash.

The other important phase for ash corrosion is K₃Al(SO₄)₃, which can lead to hot corrosion after melting at 654 °C. The reactions of this phase with high-calcium ash was discussed in our early paper [15].



The low-melting temperature phase of K₃Al(SO₄)₃ is removed after reacting with calcium containing oxides. The melting temperatures of the products of the reaction are all over 1000°C. The corrosion rate reduced after the molten phases at 750°C was removed. CaSiO₃ in high-calcium ash can also react with other low-melting temperature phases such as CoSO₄ and NiSO₄.



CoSO₄ is liquid above 735 °C. The eutectic temperature of NiSO₄- Na₂SO₄ is also below 750°C. can also form a low-melting-temperature mixture with Na₂SO₄. Corrosion rate can be affected by the formation of these low-melting phases. However, these phases can be removed if there is enough calcium containing oxides in ash. Therefore, the addition of CaO to ash can retard the formation of both low melting temperature chlorides and sulfates and minimize rapid corrosion.

4. SUMMARY

Ni-based alloys have been tested in simulated oxy-fuel environments with gases of HCl and SO₂ at 750 °C. Two types of ashes were used in this study. One ash simulates U.S. Western coal ash, which contains calcium oxide. The other simulates U.S. Eastern coal ash, which does not contain calcium oxide. Ash-based corrosion exhibit an incubation period. A chlorine-inducing mechanism is proposed according to the analysis results of synchrotron nano-beam X-ray-diffraction and SEM. Chlorine can enhance the diffusion of oxygen to into grain boundaries of

the alloys. The chromium outward diffusion can be affected by these oxides along grain boundaries. The phase composition of oxide scale changes if chlorine is present in the gas environment. A pure Cr₂O₃ does not form along the interface of metal/oxide. The incubation times for alloys decrease and their corrosion rates increase due to the presence of chlorine in the gas environment.

The long-term corrosion rate of alloys and the incubation time can be affected by calcium addition to ash. The formation of some chlorides and sulfates with low-melting-temperatures can be retarded by calcium containing oxides in ash. The removal of these low-melting-temperatures compounds change the corrosion mechanism and reduce corrosion rate. Therefore, adequate application of additives as well as judicious alloy selection can mitigate corrosion problem in oxy-fuel combustion coal power plant.

ACKNOWLEDGMENTS

This work was supported by the U.S. Department of Energy, Office of Fossil Energy, Advanced Research Materials Program, Work Breakdown Structure Element ANL-4, under Contract DE-AC02-06CH11357. Use of the Advanced Photon Source and the Center for Nanoscale Materials, an Office of Science user facility, was supported by the U.S. Department of Energy, Office of Science, Office of Basic Energy Sciences, under Contract No. DE-AC02-06CH11357.

REFERENCES

- (1) Bordenet, B. Influence of Novel Cycle Concepts on the High-temperature Corrosion of Power Plants. *Mater. Corros.* **2008**, *59*, 361-366.
- (2) Shen, J.; Zhou, L.; Li, T. High-temperature Oxidation of Fe-Cr Alloys in Wet Oxygen. *Oxid. Met.* **1997**, *48*, 347-356.
- (3) McCoy, H. E. Type 304 Stainless Steel vs Flowing CO₂ at Atmospheric Pressure and 1100-1800 F. *Corros.* **1965**, *21*, 84-94.
- (4) Zeng, Z.; Natesan, K.; Cai, Z.; Gosztola, D.; Cook, R.; Hiller, J. Effect of Element Diffusion through Metallic Networks During Oxidation of Type 321 Stainless Steel. *J. Mater. Eng. Perf.* **2014**, *23*, 1247-1262.
- (5) Stanger, R.; Wall, T. Sulphur Impacts During Pulverized Coal Combustion in Oxy-fuel Technology for Carbon Capture and Storage. *Prog. Energy Combust. Sci.* **2011**, *37*, 69-88.
- (6) Zurek, Z., Gilewicz-Wolter, J., Hetmanczyk, M., Dudala, J., and Stawiarski, A. High Temperature Corrosion of Chromium–manganese Steels in Sulfur Dioxide. *Oxid. Met.* **2012**, *78*, 1-16.
- (7) Syed, A.U.; Simms, N.J.; Oakey, J.E. Fireside Corrosion of Superheaters: Effects of Air and Oxy-firing of Coal and Biomass. *Fuel* **2012**, *101*, 62-73.
- (8) Otsuka, N. Fireside Corrosion of Austenitic Tube Materials for Advanced USC Boilers. *Mater. Sci. Forum* **2011**, *696*, 206-211.

- (9) Castello, P., Guttman, V., Farr, N., and Smith, G. Laboratory Simulated Fuel-ash Corrosion of Superheater Tubes in Coal-fired Ultra-supercritical Boilers. *Mater. Corros.* **2000**, *51*, 786-790.
- (10) Zhao, S., Xie, X., Smith, G.D., and Patel, S.J. The Corrosion of Inconel Alloy 740 in Simulated Environments for Pulverized Coal-fired Boiler. *Mater. Chem. Phys.* **2005**, *90*, 275-281.
- (11) Brossard, J.M., Diop, I., Chaucherie, X., Nicol, F., Rapin, C., and Vilasi, M. Superheater Fireside Corrosion Mechanisms in MSWI Plants: Lab-scale Study and On-site Results. *Mater. Corros.* **2011**, *62*, 543-548.
- (12) Holcomb, G.R., Tylczak, J., Meier, G. H., Lutz, B.S., Jung, K., Mu, N., Yanar, N.M., Pettit, F.S., Zhu, J., Wise, A., Laughlin, D.E., and Sridhar, S. Fireside Corrosion in Oxy-fuel Combustion of Coal. *Oxid. Met.* **2013**, *80*, 599–610.
- (13) Aung, N.N. and Liu, X. Effect of Temperature on Coal Ash Hot Corrosion Resistance of Inconel 740 Superalloy. *Corros. Sci.* **2014**, *82*, 227–238.
- (14) Zeng, Z., Natesan, K., Cai, Z., Rink, D.L. Effect of Coal Ash on the Performance of Alloys in Simulated Oxy-fuel Environments. *Fuel* **2014**, *117*, 133-145.
- (15) Z. Zeng, K. Natesan, Z. Cai, D.L. Rink, Effects of Calcium in Ash on the Corrosion Performance of Ni-based Alloys in Simulated Oxy-fuel Environment. *Fuel* **2016**, *178*, 10-22.
- (16) Z. Zeng, K. Natesan, Z. Cai, D.L. Rink, Corrosion Performance of Fe-Based Alloys in Simulated Oxy-Fuel Environment. *Metall. Mater. Trans. B* , **2017**, *48*, 642-654.
- (17) Tillman, D. A.; Duong, D.; Miller, B. Chlorine in Solid Fuels Fired in Pulverized Fuel Boilers Sources, Forms, Reactions, and Consequences: a Literature Review. *Energy Fuels* **2009**, *23*, 3379– 3391.
- (18) Chou, M. I. M.; Lytle, J. M.; Kung, S. C.; and Ho, K. K. Corrosivities in a Pilot-scale Combustor of a British and Two Illinois Coals with Varying Chlorine Contents. *Fuel Process. Technol.* **1999**, *64*, 167–176.
- (19) Nielsen, H. P.; Frandsen, F. J.; Dam-Johansen, K.; Baxter, L.L. The Implications of Chlorine-associated Corrosion on the Operation of Biomass-fired Boilers. *Progress in Energy and Combustion Science* **2000**, *26*, 283–298.
- (20) Nielsen, H. P.; Frandsen, F. J.; Dam-Johansen, K. Lab-scale Investigations of High-Temperature Corrosion Phenomena in Straw-fired Boilers. *Energy Fuels* **1999**, *13* (6), 1114–1121.
- (21) Antunes, R. A. and de Oliveira, M. C. L. Corrosion in Biomass Combustion: A Materials Selection Analysis and Its Interaction with Corrosion Mechanisms and Mitigation Strategies. *Corros. Sci.* **2013**, *76*, 6–26.
- (22) Ja'baz, I.; Chen, J.; Etschmann, B.; Ninomiya, Y. and Zhang, L. High Temperature Tube Corrosion upon the Interaction with Victorian Brown Coal Fly Ash under the Oxy-fuel Combustion Condition. *Proc. Combust. Inst.* **2017**, *36* (3), 3941–3948.

- (23) Schofield, K. A New Method to Minimize High-Temperature Corrosion Resulting from Alkali Sulfate and Chloride Deposition in Combustion Systems. I. Tungsten Salts. *Energy Fuels* **2003**, *17*, 191–203.
- (24) Schofield, K. New Method to Minimize High-Temperature Corrosion Resulting from Alkali Sulfate and Chloride Deposition in Combustion Systems. II. Molybdenum Salts. *Energy Fuels* **2005**, *19*, 1898–1905.
- (25) Kassman, H.; Pettersson, J.; Steenari, B.-M.; Åmand, L.-E. Two Strategies to Reduce Gaseous KCl and Chlorine in Deposits during Biomass Combustion –Injection of Ammonium Sulphate and Co-combustion with Peat. *Fuel Process. Technol.* **2013**, *105*, 170–180.
- (26) Liu, K.; Xie, W.; Li, D.; Pan, W.; Riley, J.; Riga, A. The Effect of Chlorine and Sulfur on the Composition of Ash Deposits in a Fluidized Bed Combustion System. *Energy & Fuels* **2000**, *14*, 963-972.
- (27) Paneru, M.; Stein-Brzozowska, G.; Maier, J.; Scheffknecht, G. Corrosion Mechanism of Alloy 310 Austenitic Steel beneath NaCl Deposit under Varying SO₂ Concentrations in an Oxy-fuel Combustion Atmosphere. *Energy Fuels* **2013**, *27*(10), 5699–5705.
- (28) Ja'baz, I.; Jiao, F.; Wu, X.; Yu, D.; Ninomiya, Y.; Zhang, L. Influence of Gaseous SO₂ and Sulphate-bearing Ash Deposits on the High-temperature Corrosion of Heat Exchanger Tube during Oxy-fuel Combustion. *Fuel Process. Technol.* **2017**, *167*, 193–204.
- (29) Aho, M.; Silvennoinen, J. Preventing Chlorine Deposition on Heat Transfer surfaces with Aluminium–silicon Rich Biomass Residue and Additive. *Fuel* **2004**, *83*(10), 1299–1305.
- (30) Aho, M.; Ferrer, E. Importance of Coal Ash Composition in Protecting the Boiler against Chlorine Deposition during Combustion of Chlorine-rich Biomass. *Fuel* **2005**, *84* (2–3), 201–212.
- (31) Schofield, K. The Chemical Nature of Combustion Deposition and Corrosion: The Case of Alkali Chlorides. *Combust. Flame* **2012**, *159*(5), 1987–1996.
- (32) Wall, T.; Liu, Y.; Spero, C.; Elliott, L.; Khare, S.; Rathnam, R.; Zeenathal, F.; Moghtaderi, B.; Buhre, B.; Sheng, C.; Gupta, R.; Yamada, T.; Makino, K.; Yu, K. An Overview on Oxy-fuel Coal Combustion—State of the Art Research and Technology Development. *Chem. Eng. Res. Des.* **2009**, *87* (8), 1003-1016.
- (33) Stein-Brzozowska, G., Maier, J., and Scheffknecht, G. Impact of the Oxy-fuel Combustion on the Corrosion Behavior of Advanced Austenitic Superheater Materials. *Ener. Procedia* **2011**, *4*, 2035-2042.
- (34) Yudovich, Y. E.; Ketris, M. P. Selenium in coal: A review. *Coal Geology* **2006**, *67*, 127–144.
- (35) Farrow, R. L.; Benner, R. E.; Nagelberg, A. S.; Mattern, P. L. Characterization of Surface Oxides by Raman Spectroscopy. *Thin Solid Films* **1980**, *73*, 353-358.
- (36) Thierry, D.; Persson, D.; Leygraf, C.; Delichere, D.; Joiret, S.; Pallotta, C.; Hugot-Le Goff, A. In-Situ Raman Spectroscopy Combined with X-Ray Photoelectron Spectroscopy and

- Nuclear Microanalysis for Studies of Anodic Corrosion Film Formation on Fe-Cr Single Crystals. *J. Electrochem. Soc.* **1988**, *135*, 305.
- (37) Maroni, V. A.; Melendres, C. A.; Kassner, T. F.; Kumar, R.; Siegel, S. Spectroscopic Characterization of Oxide Films on Type 304 SS Exposed to Water at 289° C: Correlation with the Fe-Cr-H₂O Pourbaix Diagram. *J. Nuclear Materials* **1990**, *172*, 13-18.
- (38) Thibeau, R. J.; Brown, C. W.; Heidersbach, R. H.; Raman Spectra of Possible Corrosion Products of Iron. *Appl. Spec.* **1978**, *32*, 532-535.
- (39) Grabke, H. J. Reese, E. Spiegel, M. The Effects of Chlorides, Hydrogen Chloride and Sulfur Dioxide in the Oxidation of Steels below Deposits. *Corros. Sci.* **1995**, *37*, 1023-1043.
- (40) Janz, G. J.; Bansal, N. P. Molten Salts Data: Diffusion Coefficients in Single and Multi-Component Salt Systems. *J. Phys. Chem. Ref. Data* **1982**, *11(3)*, 505-693.
- (41) Minh N. Q., Welch, B. J. The Reduction of HCl Dissolved in LiCl-KCl Eutectic. *Aust. J. Chem.* **1975**, *28*, 965-73.
- (42) Rouse, J. W.; Helms, C. R.; Deal, B. E.; Razouk, R. R.; Auger Sputter Profiling and Secondary Ion Mass Spectrometry Studies of SiO₂ Grown in O₂/HCl Mixtures. *J. Electrochem. Soc.: Solid-state Science and Technology* **1984**, *131*, 887-894.
- (43) Zeng, Z.; Natesan, K.; Cai, Z.; and Darling, S.B. The role of metal nanoparticles and nanonetworks in alloy degradation. *Nature Mater.* **2008**, *7*, 641-646.
- (44) Schmidt, A.; Lerch, M.; Eufinger, J.P.; Janek, J.; Tranca, I.; Islam, M.M.; Bredow, T.; Dolle, R.; Wiemhöfer, H. D.; Boysen, H.; Hölzel, M. Chlorine ion mobility in Cl-mayenite (Ca₁₂Al₁₄O₃₂Cl₂): An investigation combining high-temperature neutron powder diffraction, impedance spectroscopy and quantum-chemical calculations. *Solid State Ionics* **2014**, *254*, 48-58.

Figure Captions

- Figure 1. Schematic of steam and gas flow schemes used for ash experiments.
- Figure 2. Weight loss for alloys after exposure to Ash E in Gas A (Without HCl) and Gas B (with HCl) at 750 °C.
- Figure 3. Incubation times for several alloys after exposure to Ash E in Gas A (Without HCl) and Gas B (with HCl) at 750 °C.
- Figure 4. Photograph of Alloy 740 and 693 and weight loss graph of Alloy 740 after exposure to the Ash E in Gas B at 750 °C for 2400 h.
- Figure 5. Corrosion rate data (calculated after subtraction of incubation time) for alloys after exposure to Ash E in Gas A (Without HCl) and Gas B (with HCl) at 750 °C.
- Figure 6. SEM micrographs of Alloy 740 after exposure to Ash E in gas with HCl (left) and without HCl (right) at 750 °C for 1200 h.
- Figure 7. Energy-dispersive X-ray spectroscopy of cross section of Alloy 740 and mapping for several alloy/scale constituents. The alloy was exposed to Ash E and Gas B (with HCl) at 750°C for 1200 h. A BSE image of region shown in center.
- Figure 8. X-ray fluorescence of Alloy 740 after exposure to Ash E and Gas B (with 200ppm HCl) at 750 °C for 1200 h.
- Figure 9. X-ray diffraction at various locations from surface on cross section of Alloy 740 after exposure to Gas B (with 200ppm HCl) at 750 °C for 1200 h.
*: (Ni, Cr, Co, Fe)₃O₄ spinel; ∇: Cr₂O₃; ◇: Austenitic matrix.
- Figure 10. Raman scattering from oxide scale on Alloy 740 after exposure to Ash E and Gas B at 750 °C for 1200 h. Red: outer scale; Green: inner scale.
- Figure 11. X-ray fluorescence of Ni and Co at various locations from surface in the cross section of Alloy 740 after exposure to Gas B (with 200ppm HCl) at 750 °C for 1200 h.
- Figure 12. A: model for active oxidation. Nanopores open. Gases of Cl₂ and chlorides diffuse through nano-pores in oxide scale; B: Nano-pores are filled with KCl-K₂SO₄ molten salt. C: Nano-pores are filled with K₃Al(SO₄)₃.
- Figure 13. Weight loss for alloys after exposure to Ash W in Gas B (with HCl) at 750 °C.
- Figure 14. A comparison of incubation times for several alloys after exposure to Ash E (without CaO) and Ash W (with CaO) in Gas B (with HCl) at 750 °C.
- Figure 15. A comparison of corrosion rate data (calculated after subtraction of incubation time) for alloys after exposure to Ash E (without CaO) and Ash W (with CaO) in Gas B (with HCl) at 750 °C.

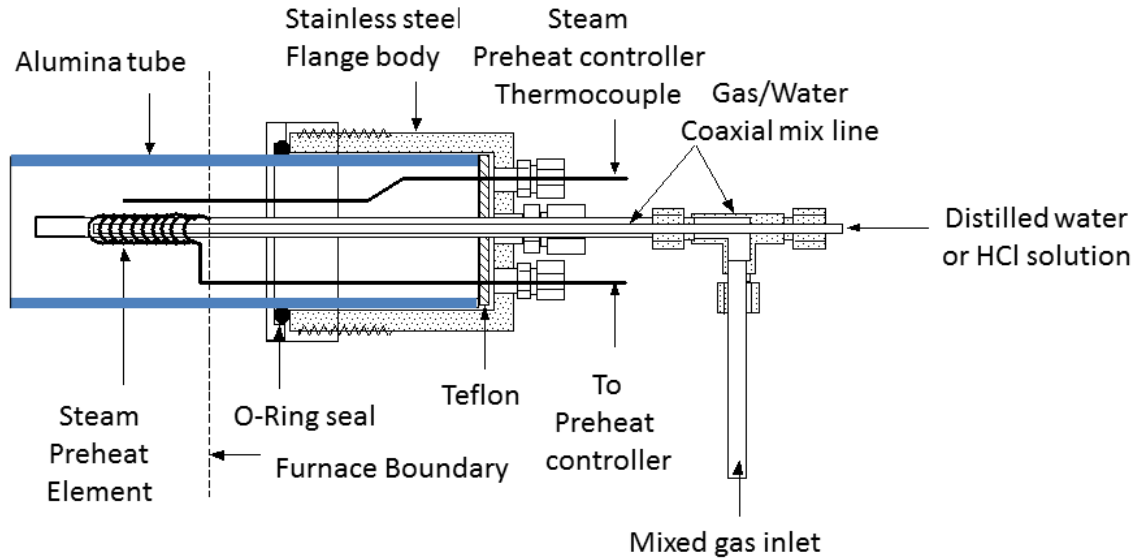


Figure 1. Schematic of steam and gas flow schemes used for ash experiments.

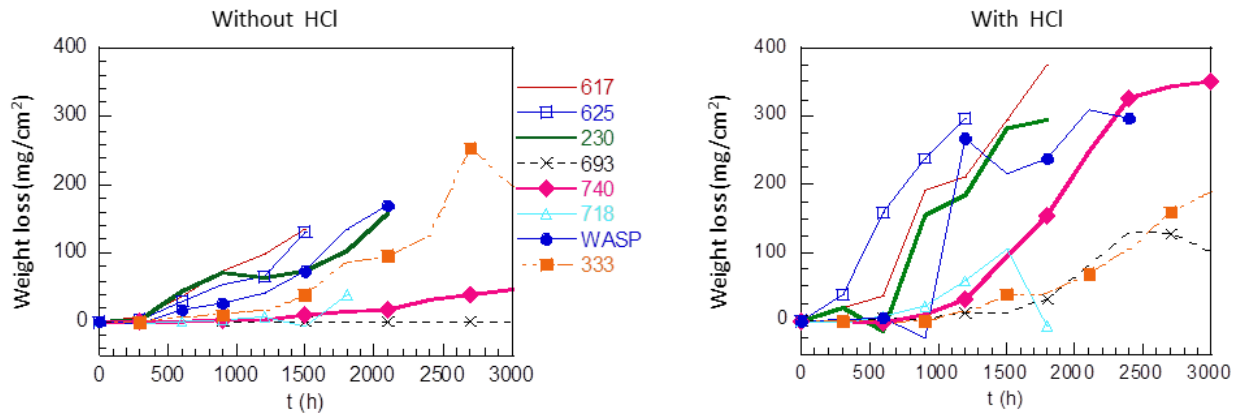


Figure 2. Weight loss for alloys after exposure to Ash E in Gas A (Without HCl) and Gas B (with HCl) at 750°C.

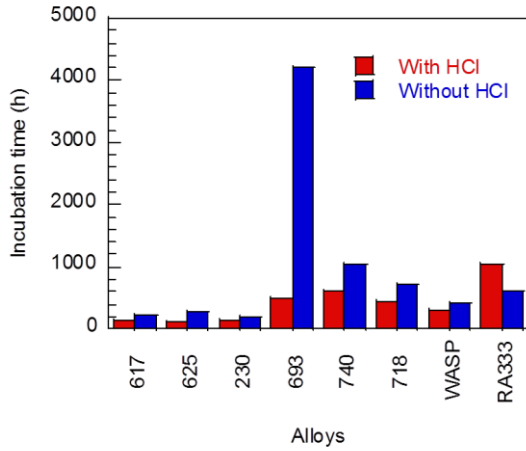


Figure 3. Incubation times for several alloys after exposure to Ash E in Gas A (Without HCl) and Gas B (with HCl) at 750°C.

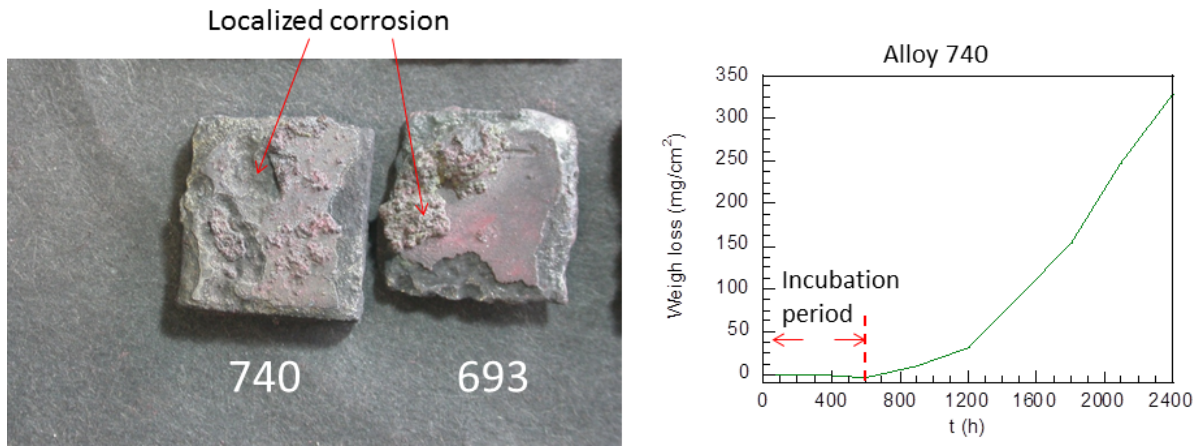


Figure 4. Photograph of Alloy 740 and 693 and weight loss graph of Alloy 740 after exposure to the Ash E in Gas B at 750°C for 2400 h.

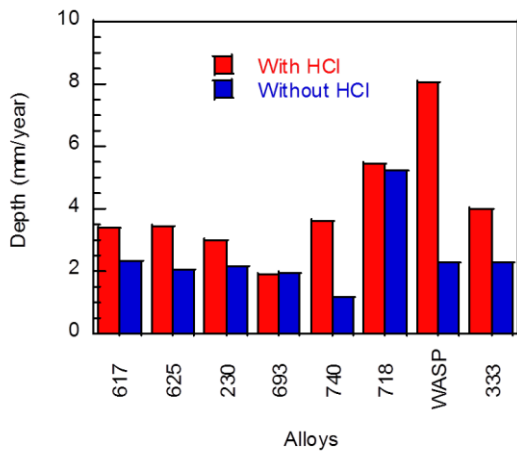


Figure 5. Corrosion rate data (calculated after subtraction of incubation time) for alloys after exposure to Ash E in Gas A (Without HCl) and Gas B (with HCl) at 750°C.

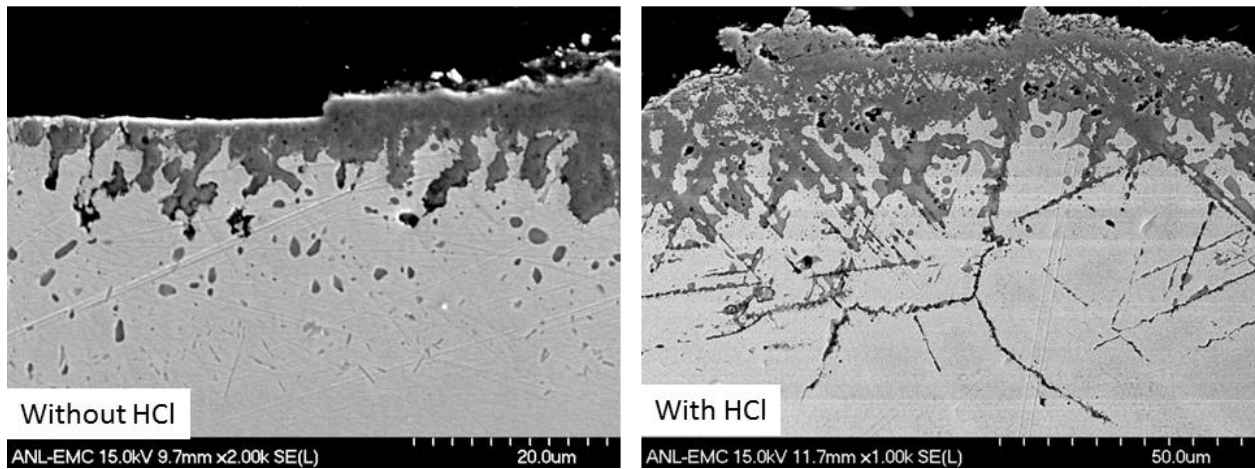


Figure 6. SEM micrographs of Alloy 740 after exposure to Ash E in gas with HCl (left) and without HCl (right) at 750 °C for 1200 h.

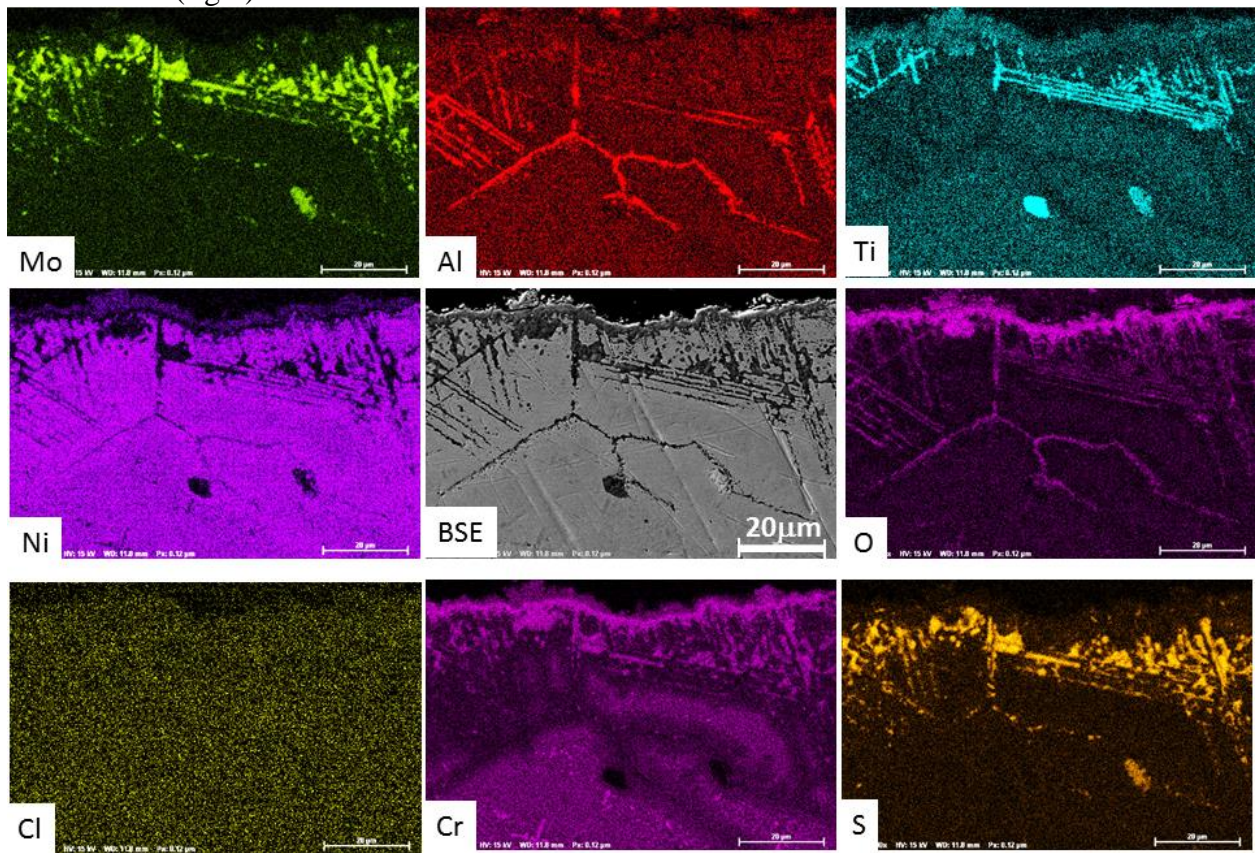


Figure 7. Energy-dispersive X-ray spectroscopy of cross section of Alloy 740 and mapping for several alloy/scale constituents. The alloy was exposed to Ash E and Gas B (with HCl) at 750°C for 1200 h. A BSE image of region shown in center.

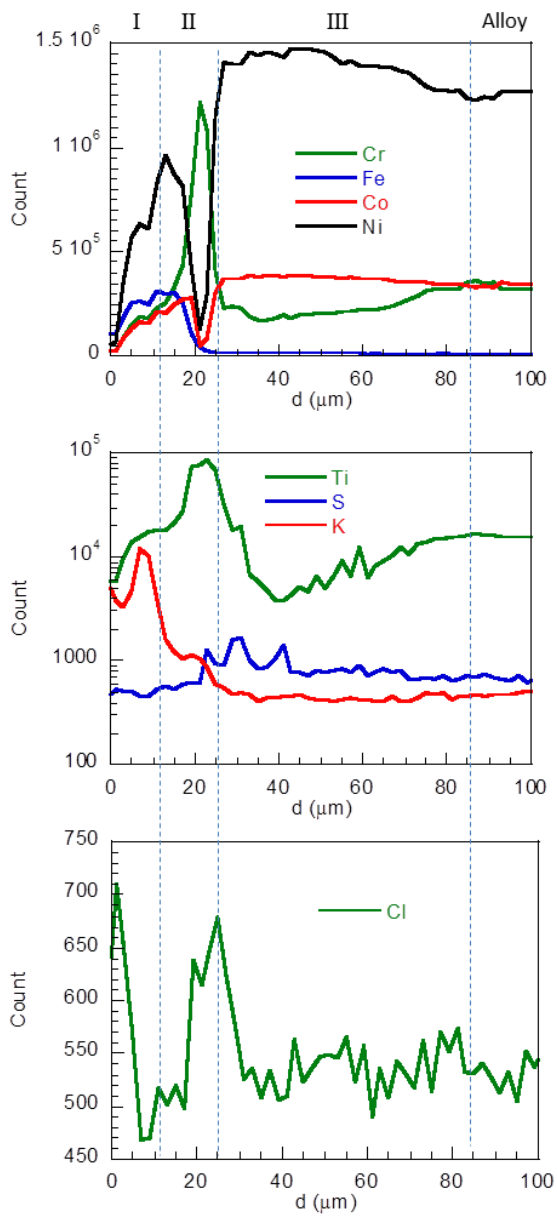


Figure 8. X-ray fluorescence of Alloy 740 after exposure to Ash E and Gas B (with 200ppm HCl) at 750°C for 1200 h.

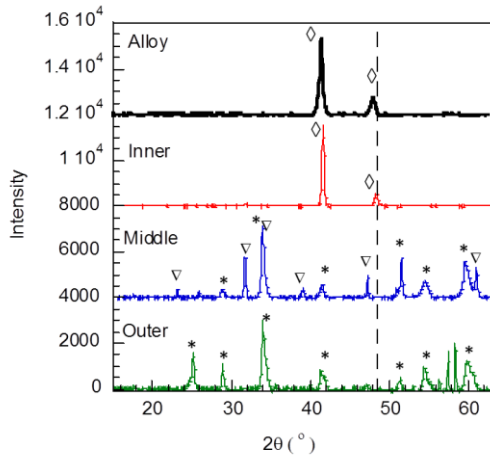


Figure 9. X-ray diffraction at various locations from surface on cross section of Alloy 740 after exposure to Gas B (with 200ppm HCl) at 750°C for 1200 h.

*: $(\text{Ni, Cr, Co, Fe})_3\text{O}_4$ spinel; ∇ : Cr_2O_3 ; \diamond : Austenitic matrix.

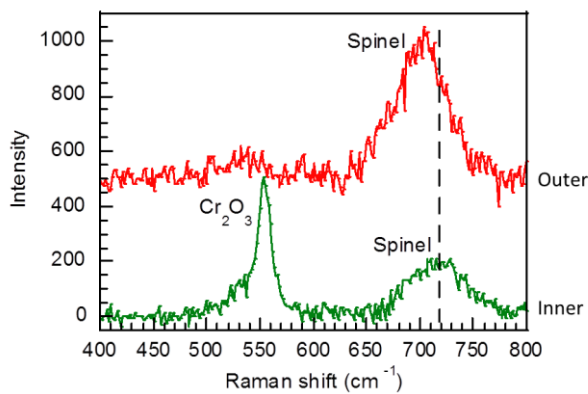


Figure 10. Raman scattering from oxide scale on Alloy 740 after exposure to Ash E and Gas B at 750 °C for 1200h. Red: outer scale; Green: inner scale.

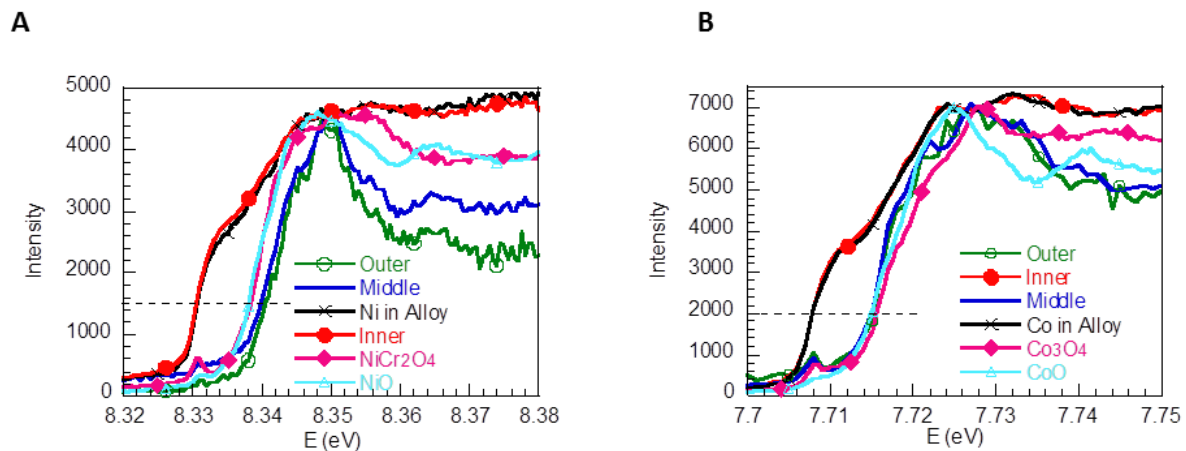


Figure 11. X-ray fluorescence of Ni and Co at various locations from surface in the cross section of Alloy 740 after exposure to Gas B (with 200ppm HCl) at 750°C for 1200 h.

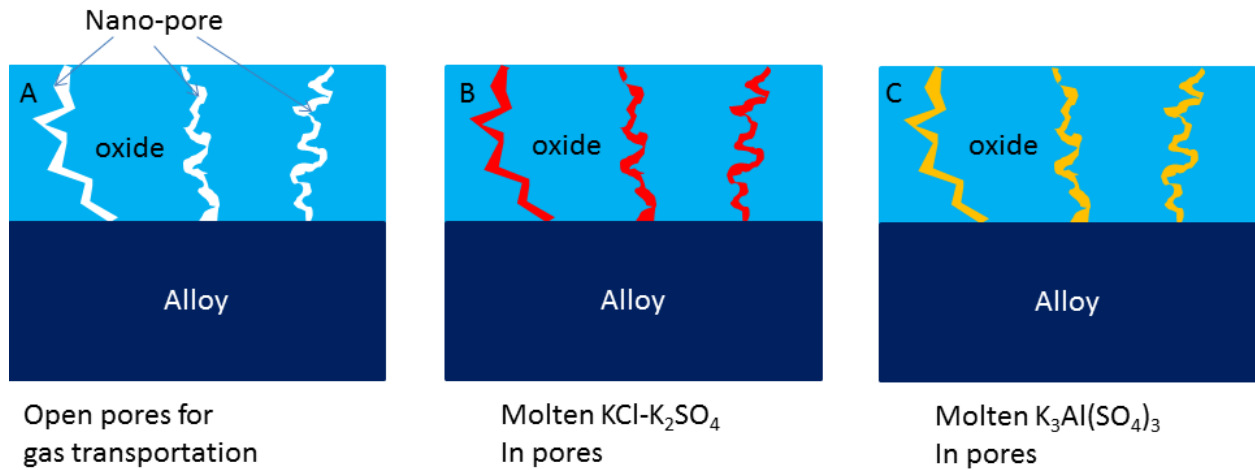


Figure 12. A: model for active oxidation. Nanopores open. Gases of Cl₂ and chlorides diffuse through nano-pores in oxide scale; B: Nano-pores are filled with KCl-K₂SO₄ molten salt. C: Nano-pores are filled with K₃Al(SO₄)₃.

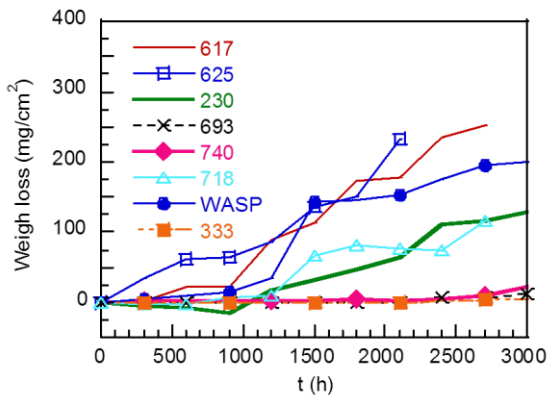


Figure 13. Weight loss for alloys after exposure to Ash W in Gas B (with HCl) at 750°C.

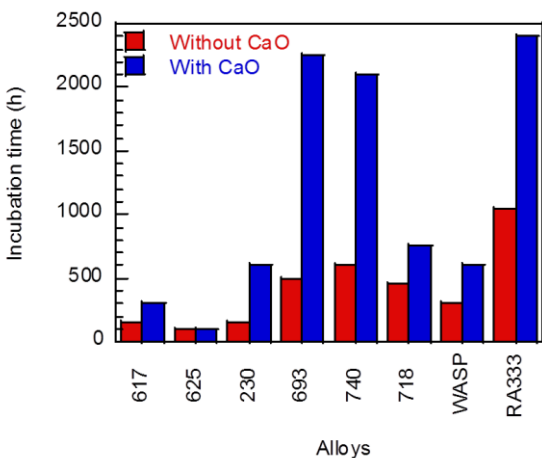


Figure 14. A comparison of incubation times for several alloys after exposure to Ash E (without CaO) and Ash W (with CaO) in Gas B (with HCl) at 750°C.

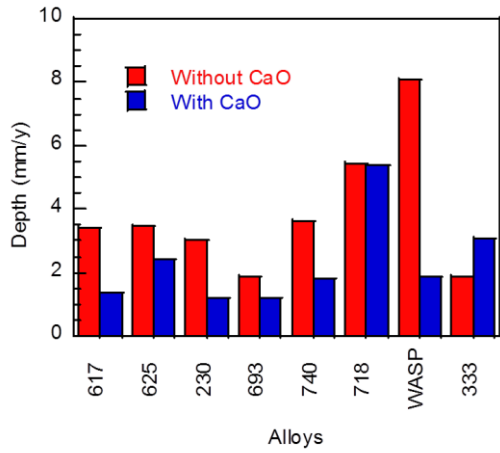


Figure 15. A comparison of corrosion rate data (calculated after subtraction of incubation time) for alloys after exposure to Ash E (without CaO) and Ash W (with CaO) in Gas B (with HCl) at 750°C.